Localization of magnetic circular dichroic spectra in transmission electron microscopy experiments with atomic plane resolution

Ján Rusz,[1,*] Jakob Spiegelberg,[1] Shunsuke Muto,[2] Thomas Thersleff,[3] Masahiro Ohtsuka,[4] Klaus Leifer,[5] and Peter M. Oppeneer[1]

[1]*Department of Physics and Astronomy, Uppsala University, P.O. Box 516, 75120 Uppsala, Sweden*

[2]*Electron Nanoscopy Section, Advanced Measurement Technology Center, Institute of Materials and Systems for Sustainability, Nagoya University, Furo-cho, Chikusa-ku, Nagoya 464-8603, Japan*

[3]*Department of Materials and Environmental Chemistry, Stockholm University, Svante Arrhenius väg 16C, 106 91 Stockholm, Sweden*

[4]*Department of Materials Physics, Graduate School of Engineering, Nagoya University, Furo-cho, Chikusa-ku, Nagoya 464-8603, Japan*

[5]*Department of Engineering Sciences, Uppsala University, P.O. Box 534, 75121 Uppsala, Sweden*

(Received 14 March 2017; revised manuscript received 13 April 2017; published 8 May 2017)

Inelastic electron scattering is a consequence of mostly Coulomb interaction between electrons in the sample and electron beam and, as such, it is a nonlocal event. In atomic resolution experiments, it thus opens the following question: How far is the origin of the inelastic scattering signal that is observed when the electron beam is passing nearby an atomic column or plane? We analyze computationally the delocalization of the magnetic signal in electron magnetic circular dichroism (EMCD) experiments in the so-called three-beam orientation, allowing one to image individual atomic planes. We compare the classical EMCD setup using the double-difference procedure (DD-EMCD) to a recently introduced atomic plane resolution EMCD (APR-EMCD) geometry, assuming the same probe size. We observe a strong localization of the EMCD signal to the closest atomic plane, confirming the potential of EMCD to study an evolution of magnetic properties near surfaces or interfaces with atomic plane resolution. The localization of the EMCD signal is remarkably higher than the localization of the nonmagnetic component of the inelastic scattering cross section. We also analyze double-channeling effects and find them particularly strong for the DD-EMCD method, while for APR-EMCD they appear to be minor. The DD-EMCD signal, on the other hand, appears to be more robust with respect to sample thickness than that of the APR-EMCD.

DOI: 10.1103/PhysRevB.95.174412

I. INTRODUCTION

Inelastic electron scattering in transmission electron microscopy is a consequence of mostly Coulomb interaction between the electrons of the sample and electrons in the beam. Although the likelihood of scattering decreases as the distance between the beam electron and the atom increases, there is a non-negligible probability that a passing beam electron can excite an atom from a distance of the order of 1 Å. This so-called delocalization of inelastic electron scattering is usually negligible, except for experiments performed at atomic resolution [1–5]. Since magnetic studies of materials utilizing inelastic electron scattering in transmission electron microscopy [6] are approaching the atomic resolution, the question of the degree of localization of the observed signal naturally emerges: Is it possible to observe magnetism with an actual atomic spatial resolution? What is the spatial area of the sample that non-negligibly contributes with magnetic signal to an electron energy loss spectrum detected by an atomic-size electron beam? Answers to these questions are important for understanding the physical limits of the actual achievable spatial resolution in magnetic studies.

Electron magnetic circular dichroism (EMCD) [6] allows one to extract the ratio of orbital and spin moment of magnetic elements in a way similar to established x-ray-based experiments. EMCD spectra are measured with transmission electron microscopes (TEMs), offering thus a spatial resolution superior to their x-ray counterpart. Recently, the first EMCD experiments with an atomic-size electron probe have been reported [7–9]. Although the EMCD signal has not yet been extracted from individual atomic columns due to inherently low signal-to-noise ratios, utilization of scanning TEM (STEM) offers a flexibility to shape the studied area and narrow it around the region of interest, for example, the interface of two materials or surfaces of nanocrystals or grains. To properly interpret such future experiments, it is important to understand the degree of localization of the inelastic (magnetic and nonmagnetic) electron scattering signal detected in the neighborhood of specific atomic columns or planes in the sample.

Here, we focus on an experimental geometry called the three-beam orientation [10,11], where the zone axis of the sample is tilted from the incoming beam by approximately 10 degrees within a plane perpendicular to a selected reciprocal lattice vector $\mathbf{G}$. As a sample, we consider the usual model system, a body-centered-cubic iron crystal which is oriented in the three-beam orientation with $\mathbf{G} = (110)$. As a consequence, the plane-wave diffraction pattern consists of a row of Bragg spots, i.e., the so-called systematic row of reflections. The systematic row of reflections consists of integer multiples of the chosen reciprocal lattice vector $\mathbf{G}$.

In this paper, we study the signal delocalization within two experimental approaches to the measurement of EMCD spectra: (1) a classical EMCD measurement [6,9,12], and (2) the recently developed atomic plane resolution EMCD (APR-EMCD) [8], both using an aberration-corrected electron probe of atomic size.

In the classical EMCD in three-beam orientation, the most accurate approach for extracting the magnetic signal is a double-difference (DD) procedure [10], where a usual circular

*jan.rusz@physics.uu.se

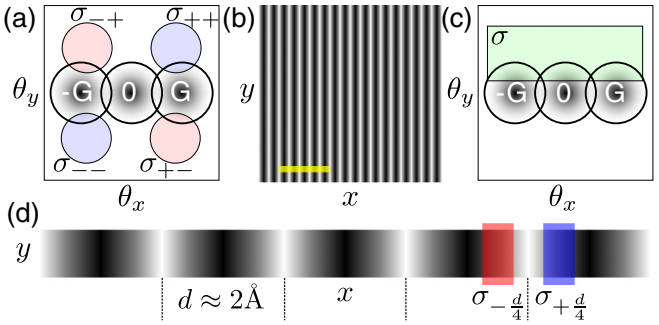

FIG. 1. Scheme of EMCD experiments in three-beam orientation with highly convergent electron beams. (a) Diffraction disks and placement of circular detector apertures for a classical EMCD experiment. (b) High-angle annular dark-field (HAADF) image showing white stripes at the positions of the atomic planes. The yellow bar represents the region to which we zoom into in (d). Here its width corresponds to approximately 1 nm. (c) Diffraction disks and placement of rectangular detector aperture for the APR-EMCD experiment. (d) Zoom-in of the HAADF image, marking positions of atomic planes (vertical dashed lines) and spectral summation areas for APR-EMCD (colored rectangles). See text for details about the notation of σ.

detector aperture is placed inside a quadrant of the diffraction pattern. Often, especially for larger convergence angles, it appears advantageous to place it in the neighborhood of the Bragg scattered beam **G** [9,10,13]. In this approach, one should scan the same area four times, placing the detector symmetrically to all four quadrants, and the EMCD is extracted as a "double difference",

$$\mathrm{EMCD} = [\sigma_{++} - \sigma_{+-}] - [\sigma_{-+} - \sigma_{--}], \tag{1}$$

where the subscript refers to the signs of the scattering angles defining the orientation of the detector, θ_x,θ_y; see Fig. 1(a).

Compared to DD-EMCD, the advantage of APR-EMCD is that the magnetic signal can be extracted from a single scan. Assuming that the systematic row of reflections is aligned with the x axis of the diffraction pattern, a rectangular detector is placed to the upper or lower diffraction half plane, above or below the systematic row of reflections, horizontally centered at the transmitted beam; see Fig. 1(c). If we denote the lattice spacing parallel to the systematic row vector **G** by $d_{(110)}$, then the EMCD signal is extracted from areas displaced by $\pm\frac{1}{4}d_{(110)}$ from the lattice planes,

$$\mathrm{EMCD} = \sigma_{+\frac{d}{4}} - \sigma_{-\frac{d}{4}}, \tag{2}$$

where σ is the measured inelastic scattering cross section and the subscript $\pm\frac{d}{4}$ refers to the scan area from which the cross section is extracted; see Figs. 1(b) and 1(d). Here, $d \equiv d_{(110)} = \frac{\sqrt{2}a}{2} = 2.03$ Å, where $a = 2.87$ Å is the lattice parameter of the bcc iron.

II. METHOD AND COMPUTATIONAL DETAILS

The model system, for which all simulations have been performed, is a bcc iron crystal with lattice parameter $a = 2.87$ Å. It is oriented in a three-beam orientation with $\mathbf{G} = (110)$ and a tilt from (001) zone axis of approximately ten degrees. Since

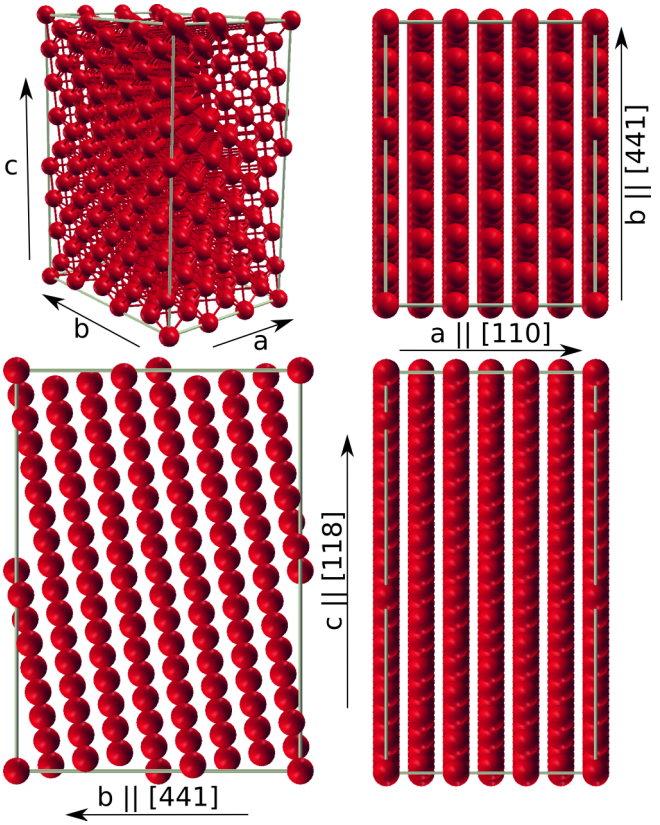

FIG. 2. Orthogonal supercell of a bcc iron oriented in three-beam orientation. A perspective projection (top left) is complemented with the three planar projections.

the multislice part of our simulation code requires orthogonal structures and prevents us from using large tilt angles, we have constructed a large supercell with 396 atoms, which has its c-axis parallel to $(\bar{1}18)$. The a and b axes were parallel to $\mathbf{G} = (110)$ and $(4\bar{4}1)$, respectively. Along the a axis, we have tripled the minimal orthogonal supercell to have enough space to study localization of signals along specific atomic planes. In this way, there are six independent atomic planes and the periodic boundary conditions are applied after every $3\sqrt{2}a = 1.22$ nm—comfortably more than the expected delocalization of the inelastic scattering signal. This leads to a supercell volume of $3\sqrt{2}a \times \sqrt{33}a \times \sqrt{66}a = 198a^3$. A perspective image and side views of this supercell are shown in Fig. 2.

The supercell was discretized on a grid of $192 \times 260 \times 350$ grid points for the multislice calculation. The supercell was repeated 4×3 times in the lateral directions to avoid overlaps of the electron-beam wave function with its periodic images. Along the z axis, the supercell was periodically repeated as many times as the target thickness required. In this work, we considered sample thicknesses from 4.66 to 51.3 nm with a step of 4.66 nm, which correspond to repeating the supercell 2 to 22 times.

For the inelastic scattering calculations, we used the MATS.V2 method [14], which is an evolution of the MATS [15] algorithm, combining multislice and Bloch waves method [16] and allowing one to extract individual atomic contributions [17]. The MATS.V2 convergence parameter was set to 10^{-5} and

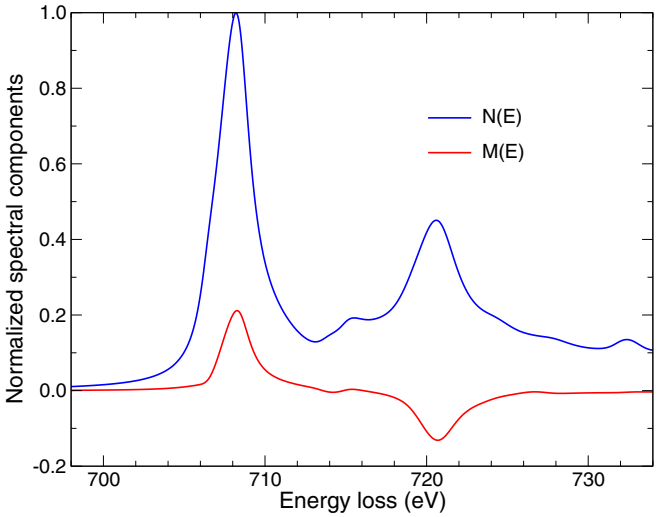

FIG. 3. The nonmagnetic $N(E)$ and magnetic (EMCD) $M(E)$ spectral components determining the mixed dynamical form factor of bcc iron in electric dipole approximation.

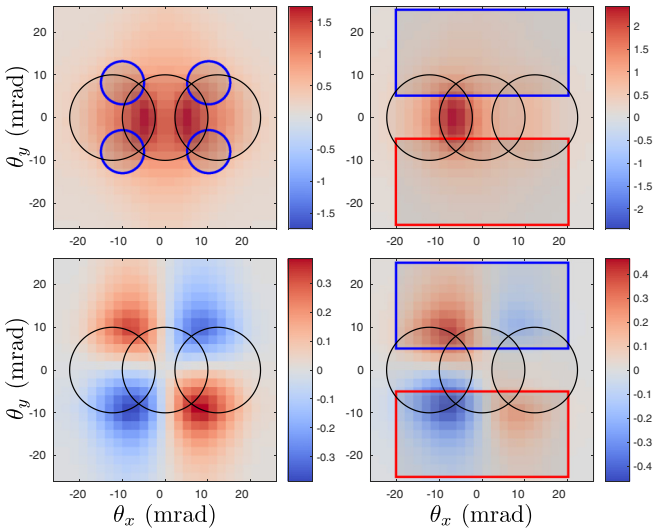

FIG. 4. Illustration of detector positions for the two studied EMCD measurement methods: DD (left) and APR (right). Top: nonmagnetic signal; bottom: EMCD. Thin black circles mark the disks corresponding to $\pm\mathbf{G}$ and 0 spots; convergence semiangle $\alpha = 10$ mrad. The calculation was done for $t = 9.33$ nm and beam position on the plane for DD and displaced by $d/4$ for APR. For APR, there are two alternative detector orientations marked by blue and red rectangles. Here we have used the blue one, in the upper diffraction half plane.

the basis size for the outgoing beam was approximately 220. Weickenmeier and Kohl scattering potentials [18] were used. The effect of atomic vibrations was included via Debye-Waller factors for iron, measured at 300 K [19]. The Fe-L_3 diffraction patterns were calculated on a grid spanning ± 25 mrad in both $\theta_{x,y}$ scattering directions, with a step of 2 mrad. For future reference, in the diffraction patterns, the θ_x scattering direction is assumed to be parallel to the systematic row index $\mathbf{G} = (110)$ and the θ_y axis passes through the center of the zero spot.

In the calculations presented below, the magnetic and nonmagnetic signal components are evaluated separately, without actual input from electronic structure calculations. We have used the electric dipole approximation, within which the mixed dynamical form factor (MDFF) can be written as [14]

$$S(\mathbf{q},\mathbf{q}',E) = \mathbf{q}\cdot\mathbb{N}(E)\cdot\mathbf{q}' + i(\mathbf{q}\times\mathbf{q}')\cdot\mathbf{M}(E), \qquad (3)$$

where $\mathbb{N}(E)$ and $\mathbf{M}(E)$ contain the electronic structure information of nonmagnetic and magnetic character, respectively. In this work, we set

$$\mathbb{N}(E) = \mathbb{1} \quad \text{and} \quad \mathbf{M}(E) = 0 \qquad (4)$$

to get the nonmagnetic signal, and

$$\mathbb{N}(E) = 0 \quad \text{and} \quad \mathbf{M}(E) = \hat{\mathbf{e}}_z \qquad (5)$$

to get the magnetic (EMCD) signal, respectively. As a consequence, the absolute values of the scattering cross sections presented below are given in arbitrary units.

Such treatment is sufficient, since the primary objective of this work is to study the delocalization of the nonmagnetic and magnetic signal components, which does not depend on the actual strength and spectral shape of $\mathbb{N}(E)$ and $\mathbf{M}(E)$. For the sake of completeness, in Fig. 3 we present the nonmagnetic and magnetic spectral shapes $N(E)$ and $M(E)$, which determine the energy dependence of the MDFF of bcc iron. Since iron has a cubic crystal structure and the spin-orbital effects within the band states are very weak, the nonmagnetic signal component tensor can be expressed as

$$\mathbf{q}\cdot\mathbb{N}(E)\cdot\mathbf{q}' \approx N(E)\mathbf{q}\cdot\mathbf{q}'. \qquad (6)$$

For the same reason, the magnetocrystalline anisotropy is very small and thus the magnetic spectral component is independent of the magnetization direction and can be represented by a single spectral dependence, $M(E)$. Specifically, here,

$$\mathbf{M}(E) = M(E)\hat{\mathbf{e}}_z \equiv [0,0,M(E)]. \qquad (7)$$

The spectral components $N(E)$ and $M(E)$ were evaluated using density functional theory, as described in Ref. [20], and broadened by Lorentzians with full width at half maximum (FWHM) of 0.7 and 1.2 eV for the L_3 and L_2 edges, respectively, to simulate finite core hole lifetime effects.

We note that although the total scattering cross section is naturally always positive, the magnetic component of the scattering cross section can be either positive or negative—depending on the range of energy losses and on dynamical diffraction conditions. Yet, it will always be dominated by the positive contribution from the nonmagnetic component.

The detector spans for the DD-EMCD method were defined as shown in the left panels of Fig. 4. The detectors were centered at scattering angles $\theta_x = \pm 10$ and $\theta_y = \pm 8$ mrad, each having a collection semiangle of 5 mrad. For the APR-EMCD, the rectangular detector aperture spanned an area with corners at $(\theta_x,\theta_y) = (-20,5)$ and $(\theta_x,\theta_y) = (20,25)$ mrad, as shown in the right panels of Fig. 4. The total areas covered by detectors were 314 and 800 mrad^2 for DD-EMCD and APR-EMCD, respectively.

Note the alternating signs of EMCD in the individual quadrants of the diffraction plane in the DD-EMCD case. This

is also visible in APR-EMCD. There, however, a superposition of DD-EMCD and APR-EMCD leads to an imbalance of the EMCD intensities in the left vs right diffraction half plane. Consequently, the summation over the rectangular detector in APR-EMCD gives nonzero EMCD strength. It is also worthwhile to mention the reduced inelastic scattering to larger scattering angles for a beam positioned $d/4$ aside the atomic plane (APR-EMCD beam position), when compared to the beam positioned directly on the atomic plane (DD-EMCD beam position).

III. CLASSICAL EMCD GEOMETRY

A. Single off-axis detector orientation

In Sec. I, we discussed that in the classical three-beam geometry, one needs to acquire four spectrum images from the same spatial area using four different detector orientations. Then, by processing these datasets using the DD procedure [10,13,21], one can isolate the EMCD signal. In the simulations, however, the nonmagnetic and magnetic contributions to the intensity of inelastically scattered electrons can be calculated separately [22]. Since this brings some interesting insight, we start our analysis of the classical EMCD geometry with data calculated for a single detector orientation. In particular, we will consider the following setup: acceleration voltage $V_{\mathrm{acc}} = 200$ kV, convergence semiangle 10 mrad, sample thickness $t = 9.33$ nm, and detector position in the top-right quadrant ($\theta_x, \theta_y > 0$), as defined in Fig. 4.

By moving the beam along the a axis (Fig. 2) and keeping track of individual atomic contributions to the total inelastic scattering cross section, we plot in Fig. 5(a) an intensity profile as a function of beam position (thick gray line), together with contributions from individual atomic planes (thin colored lines). An interesting observation stemming from this plot is that the peaks of the nonmagnetic signal are shifted from the position of atomic planes by approximately 0.4 Å. This is caused by the detector center being displaced from the $\theta_x = 0$ axis. Moving the detector to the top-left quadrant ($\theta_x \to -\theta_x$ and θ_y unchanged) gives the same shift, but in the opposite direction. On the first look, this might cause problems when using cross-correlation methods to spatially align the spectrum images. This is certainly true if we would use the spectrum images themselves for the alignment procedure. However, it is common to record a high-angle annular dark-field (HAADF) image along with the spectrum images, where the shift would not be observed [or, at least, it would not depend on the electron energy loss spectroscopy (EELS) detector orientation]. Thus, if the alignment procedure is performed using HAADF images rather than spectrum images themselves, there should be no issues due to displacement of the peaks of the nonmagnetic signal from the atomic planes. On the other hand, it would be interesting to confirm this phenomenon experimentally, i.e., to detect the small relative shift of intensity peaks between the HAADF and spectrum images.

The total intensity profile, depicted as a gray line in Fig. 5(a), allows us to define the atomic plane contrast as $1 - I_{\mathrm{min}}/I_{\mathrm{max}}$, which in the present parameter settings evaluates to approximately 50%. Thus the core level edge signal will not drop under 50% of the maximum, regardless of

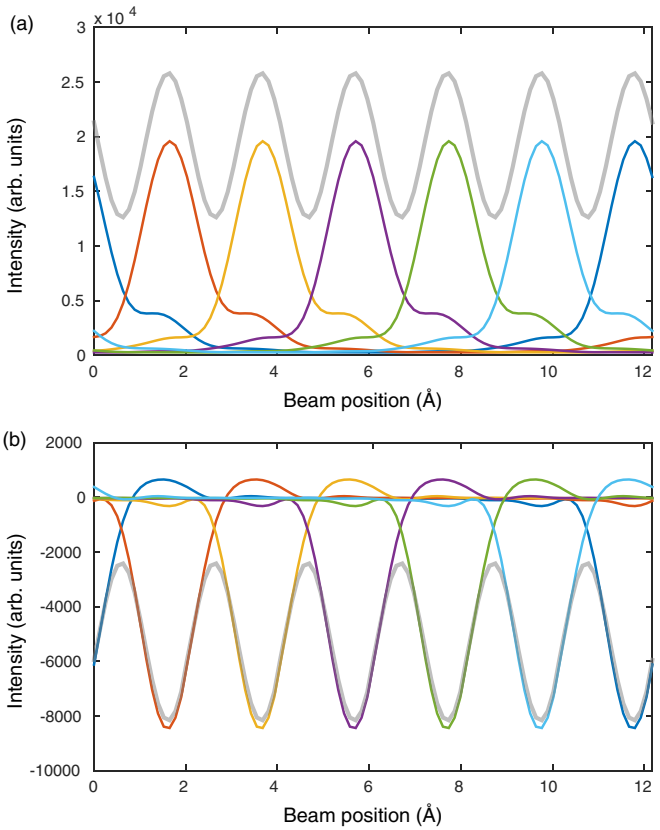

FIG. 5. Off-axis detection setup. Intensity profiles of the (a) nonmagnetic and (b) magnetic component of the inelastic scattering cross section for a probe with 10 mrad convergence semiangle and sample thickness of 9.3 nm. The thick gray line marks the total profile and colored lines mark the six individual plane contributions. A single circular detector aperture is positioned in the upper-right quadrant, $\theta_x, \theta_y > 0$.

where we position the beam. This is likely due to the relatively large beam size (FWHM is approximately 1.3 Å) when compared to the interplane spacing $d_{(110)} = 2.03$ Å, beam broadening, and channeling effects, but also the delocalization of the inelastic scattering signal.

The delocalization itself can be seen on the colored line profiles in Fig. 5(a), where the total nonmagnetic part of the scattering cross section is separated into contributions from the six atomic planes present in our structure model; see Fig. 2. The contributions of individual lattice planes are peaked with a FWHM of approximately 1.5 Å. This agrees well with qualitative expectations [23] giving the STEM-EELS resolution as $\sqrt{d_{\mathrm{probe}}^2 + d_{50}^2} = 1.54$ Å, where $d_{\mathrm{probe}} = 1.28$ Å is, in our case, a diffraction-limited probe size with zero source size and zero optical and chromatic aberrations, and $d_{50} = \frac{\lambda}{2}(\frac{E_0}{\Delta E})^{\frac{3}{4}} = 0.87$ Å is the diameter of an area around the atom within which 50% of inelastic excitations take place [24]; $\lambda = 2.5$ pm for electrons of kinetic energy $E_0 = eV_{\mathrm{acc}} =$ 200 keV and, for the L_3 edge of iron, the energy loss ΔE is approximately 700 eV.

Note the asymmetric distribution of the signal from an individual atomic plane. The shoulder on the right-hand side is substantially larger than that on the left-hand side of the

peak. (This, again, is reversed when we move the detector to the top-left quadrant.) Importantly, at the peak value of the intensity profile, almost one-quarter of the intensity comes from neighboring atomic planes, while the contributions from the next-nearest atomic planes are rather negligible. To quantify the delocalization in less ambiguous terms, we define a surrounding of an atomic plane by an interval $(-\frac{d}{8}, \frac{d}{8})$ and integrate the intensity originating from individual atomic planes. For the case depicted in Fig. 5(a), this accounts for 76%, 10.5%, 8.0%, 2.1%, 1.9%, and 1.2%, respectively, for individual atomic planes ordered in the following way: the closest first, then left nearest neighbor, right nearest neighbor, left second-nearest neighbor, right second-nearest neighbor, and, finally, the most distant plane. For the case discussed here, the delocalization is substantial among the nearest-neighboring planes; however, it appears safe to assume that the nonmagnetic signal at a certain atomic plane comes predominantly (∼95%) from the selected plane plus its two nearest neighbors.

Now we shift our attention to the EMCD signal evaluated in the same settings, shown in Fig. 5(b). The total magnetic signal profile has a negative sign for this detector orientation. The peaks of the magnetic signal are shifted from the nearest atomic plane by approximately the same amount as the nonmagnetic signal. Compared to the nonmagnetic signal, the contrast is higher here, reaching almost 70%. This suggests that the EMCD signal is more localized to its corresponding atomic plane. Indeed, peaks of the EMCD signal have a FWHM of only about 1.3 Å, proposing that the image formation based on a purely magnetic signal should follow somewhat different qualitative principles than the total (nonmagnetic) signal, where the resolution could be well estimated using simple qualitative arguments. Interestingly, the contributions from the neighboring atomic planes have an opposite sign, with the left plane contributing positively and right plane contributing negatively. The individual contributions are 102%, −6.3%, 2.3%, 0.3%, 0.9%, and 0.4%, evaluated in the same order as above for the nonmagnetic signal. Here we can observe that the EMCD signal from the second-nearest neighbors is negligible; it is thus somewhat better localized than the nonmagnetic component discussed above. This reflects the narrower FWHM of the magnetic peak belonging to a particular atomic plane, compared to the nonmagnetic one.

We note that individual atomic contributions to the nonmagnetic signal are always positive [Fig. 6(a)], while the EMCD contributions to the scattering cross section can be both positive or negative [Fig. 6(b)]. In Fig. 6, we positioned the beam at the center of an atomic plane. Note how the major contributions indeed come from the particular plane, best seen in y-projected view (middle), where the beam does not spread much to the neighboring planes. However, it spreads rather significantly *within* the atomic plane, as is best seen on x projections (left). Non-negligible contributions can come from a spread of almost 1 nm. Note how the individual nonmagnetic contributions get somewhat reduced after approximately 30 nm (middle), which is a consequence of the beam spreading. The situation is qualitatively similar also for the EMCD atomic contributions, except for the oscillating sign. These oscillations cause a mutual cancellation of the overall EMCD signal and they are the main reason why the EMCD measurements put strict limits on the sample thickness; otherwise the relative strength of EMCD signal can drop to prohibitively low values. The oscillation of the sign happens with a period of about 40 nm, which is rather close to the extinction distance $\xi_{\mathbf{G}}$ for $\mathbf{G} = (110)$, which is approximately 39 nm for an iron crystal at 200 keV. At specific sample thicknesses it may happen that the total EMCD signal is close to zero. At such values, the EMCD signal can be strongly delocalized—the contributions of several neighboring atomic planes can be of similar magnitude, though all of them are usually very weak in absolute terms. For these reasons, when studying localization of the EMCD signal within specific planes, it is more insightful to work with absolute numbers, while for the nonmagnetic signal, one can get meaningful percentages of atomic plane contributions across the whole range of considered thicknesses. We should note that one cannot *a priori* use Fig. 6 to analyze the thickness dependence of EMCD because double-channeling effects can substantially influence individual atomic contributions. This will be discussed in detail below in Sec. V.

B. Double-difference procedure

The DD procedure requires four spectrum images from the same area on the sample in order to isolate the magnetic signal from spectrum images. We will assume that these spectrum images can be spatially aligned by cross correlation of their associated HAADF images—this way we can ignore the peak shifts of the nonmagnetic signal in the individual spectrum images. The next complication that occurs is that if we take the spectrum images as calculated and perform the DD procedure, the nonmagnetic signal will be strongly suppressed, but it will not vanish entirely. For beam positions in between the atomic planes, a small amount of nonmagnetic signal remains even after the DD procedure; see Fig. 7(c). This is not entirely negligible because quantitatively it is of the same order of magnitude as the magnetic signal: in the settings considered here, the DD residuals are up to 30% of the EMCD signal strength.

In practice, this is avoided by postedge normalization, prior to the DD procedure. With this being done, the nonmagnetic signal vanishes and pure EMCD remains, slightly modified by multiplicative factors which were used for postedge normalization. For a given pixel, the four normalization factors are typically rather similar to each other, and therefore they are not likely to influence much the final EMCD signal maps. Furthermore, it is only the signal's absolute intensity which is affected by this normalization. The analysis of the EMCD spectrum itself via the sum rules [25,26] to determine, e.g., the ratio of orbital and spin magnetic moments is not impaired.

Thus, we have constructed the profile of the EMCD signal by performing a DD procedure on the net magnetic signal calculated for the four detector orientations, shown in Fig. 7(b). There are two notable differences compared to the EMCD profile from a single detector orientation [Fig. 5(b)]. First, the peaks of both the nonmagnetic and magnetic signals are located exactly at the position of the atomic planes. This is owing to mutual compensation of the shifts of peaks for the detector orientations in the left vs right diffraction half planes. Second, the contrast is much reduced: now only about

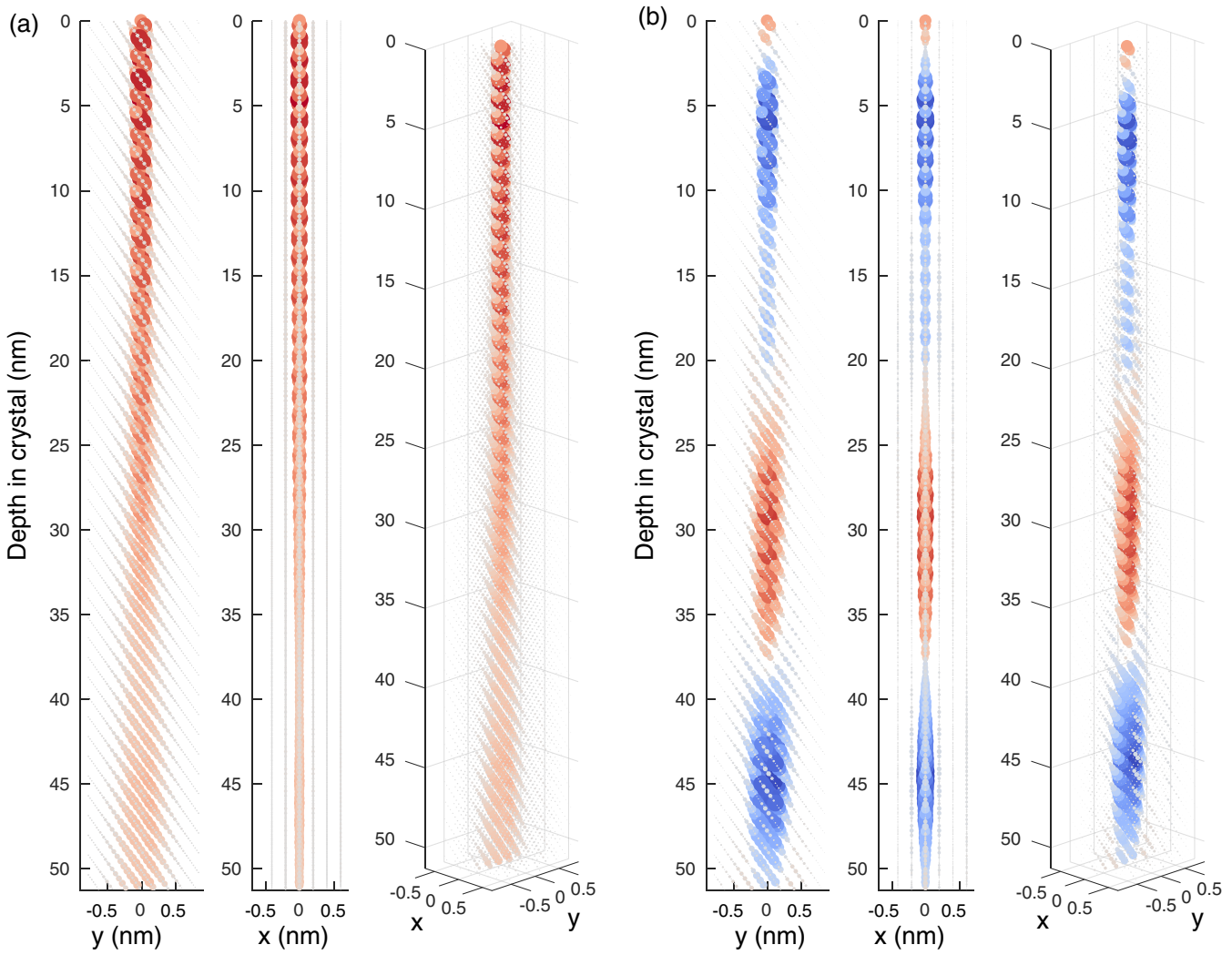

FIG. 6. Three-dimensional view of individual atomic contributions to the inelastic scattering cross section from three different angles of view. The color and size of the sphere represent the magnitude of the atomic contribution. Zero level corresponds to gray color, blue to negative, and red to positive. (a) Nonmagnetic contributions; (b) magnetic (EMCD) contributions. The image presents a DD-EMCD calculation with a 10 mrad convergent electron beam centered on an atomic plane.

30%. This is caused by overlapping slightly displaced peaks, resulting in a broader peak. Indeed, now the FWHM of a single lattice contribution to the magnetic signal is almost 1.9 Å. Yet, the localization of the magnetic signal remains excellent, the nearest-neighboring planes contribute with less than 2%, and other planes contribute negligibly.

As one would expect, the contrast (see Table I) typically improves with larger convergence angles α, both for the nonmagnetic and magnetic signal components. However, there are some situations where this simple qualitative expectation fails; see, for example, $\alpha = 15$ mrad and $t = 9.33$ nm, which has a substantially lower nonmagnetic contrast than $\alpha = 10$ mrad and $t = 9.33$ nm. Note that the detectors here do not span a typical STEM bright-field collection angle, where one collects all the electrons scattered up to certain collection angle β, which is typically set to be $\beta > \alpha$. Here, in the DD approach, the total detector span consists of four discontinuous and relatively small ranges of scattering angles. Therefore, it is natural to expect strong dynamical diffraction effects, which will move electrons in and out of these ranges as the sample thickness is increased. Due to this, there are also very strong double-channeling effects in the DD-EMCD approach, which will be discussed in Sec. V below. Apart from that, we observe strong channeling of electrons along the atomic planes and, for larger thicknesses, we observe strong beam spreading, particularly for beams with large convergence angles. Combination of these phenomena leads to sharpening of the intensity peaks at the atomic planes' positions.

The contrast of the EMCD signal behaves somewhat less erratically, i.e., it mostly improves with smaller beam, except for the largest considered thicknesses. There, however, the EMCD signal is a very low fraction of the nonmagnetic signal (see Fig. 8) and it becomes delocalized and strongly dependent on the beam position. This is likely related to a strong beam spreading, discussed above. Note also how the relative strength of the EMCD signal decreases with increasing convergence angle and sample thickness.

The localization properties of the DD procedure, both for the nonmagnetic and EMCD signals, respectively, are summarized in the upper panels of Fig. 8. The beam was

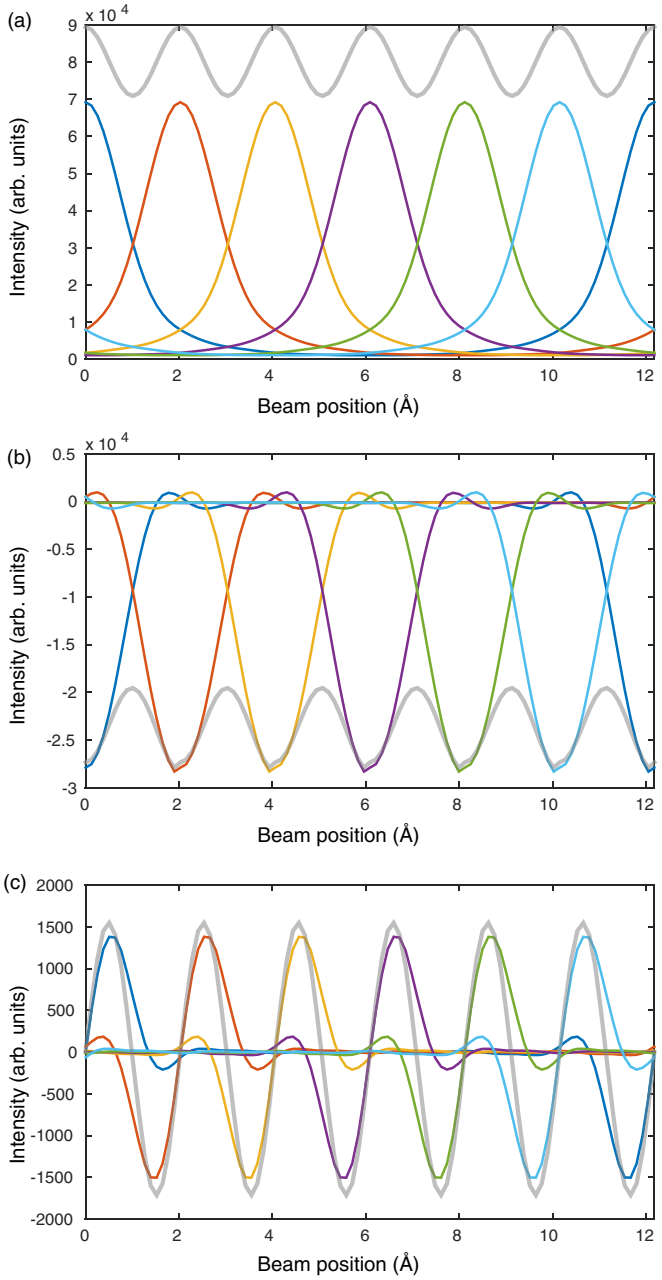

FIG. 7. Results simulated for the DD-EMCD setup. Intensity profiles of the (a) nonmagnetic, (b) magnetic component, and (c) residuum of nonmagnetic component after the double-difference procedure. Calculations were done for a probe with 10 mrad convergence semiangle and a sample thickness of 9.3 nm. The thick gray line marks the total profile and colored lines mark the six individual plane contributions. The four circular detector apertures for the double-difference procedure are marked in Fig. 4.

centered on the third atomic plane, as shown in the insets, and the spatial integration range was within $\pm\frac{d}{8}$ around the atomic plane. The nonmagnetic signal was obtained as a sum from all four detector positions, while the EMCD signal was obtained by the DD procedure.

For all of the three considered convergence angles, the nonmagnetic signal is strongly dominated by contributions from the third plane. The relative strength of this contribution remains above 80%, except for the smallest convergence angle $\alpha = 10$ mrad, where it drops to 74% at the largest thickness. Contributions from the two neighboring planes (planes 2 and 4) are under 10%, somewhat decreasing with increasing convergence angle. Contributions of other planes seem negligible, typically under 3%.

For the magnetic signal, the qualitative picture is more intricate due to the oscillating signs of individual atomic contributions; see Fig. 6. Therefore, in Fig. 8, we show absolute values of the atomic plane contributions to the EMCD signal. It is immediately clear that the EMCD signal from plane 3 strongly dominates the total EMCD, except for the cases when it approaches values close to zero. While at $\alpha = 10$ mrad the EMCD signal from the third plane remains non-negligible across the whole range of thicknesses, at $\alpha =$ 15 and 20 mrad it approaches zero at thicknesses near 30 nm. At these thicknesses, naturally, the fractional contribution from other atomic planes increases significantly, though that is of little practical relevance because the EMCD signal is simply very weak at such thicknesses. Except for these situations, the EMCD signal in the DD-EMCD remains remarkably dominated by contributions from the atomic plane, through which the beam is passing. This suggests that atomic resolution EMCD measurements in the DD-EMCD setup should give an access to truly local modifications of magnetic properties, plane by plane.

IV. ATOMIC PLANE RESOLUTION EMCD

In this section, we discuss the APR-EMCD setup, which has a number of practical advantages over the DD approach. The most important of them is that the EMCD signal can be extracted from a single spectrum image. There is no need to scan the same area multiple times because the magnetic signals of positive and negative signs are both present in the same dataset at beam positions known in advance.

As in the case of the DD procedure, here we will discuss the contrast and localization of the EMCD and nonmagnetic components of the inelastic scattering cross section. We will discuss in detail the same particular case ($\alpha = 10$ mrad, $V_{\mathrm{acc}} =$ 200 kV, $t = 9.33$ nm), and the results of an exploration of the parameter space are summarized in Table I and in the bottom panels of Fig. 8.

Figure 9(a) shows the dependence of the nonmagnetic signal on the beam position. The gray line represents the total signal, which shows a contrast of approximately 35%. This is a lower contrast, when compared to Fig. 5(a); however, it is comparable to the contrast observed for the DD procedure [Fig. 7(a)] when the nonmagnetic signals from all four quadrants are summed together. Importantly, in the APR-EMCD, the peak positions coincide with the location of the atomic planes, i.e., no shift is observed. This is because in APR-EMCD, the detector spans an area that is symmetric with respect to the $\theta_x = 0$ axis.

Contributions of the individual lattice planes to the total nonmagnetic signal follow a simple peak with a FWHM of approximately 1.6 Å, having relatively large tails that contribute to the intensity centered at the neighboring plane by approximately 7% of the total. In total, about 18% of the intensity observed at a particular atomic plane actually

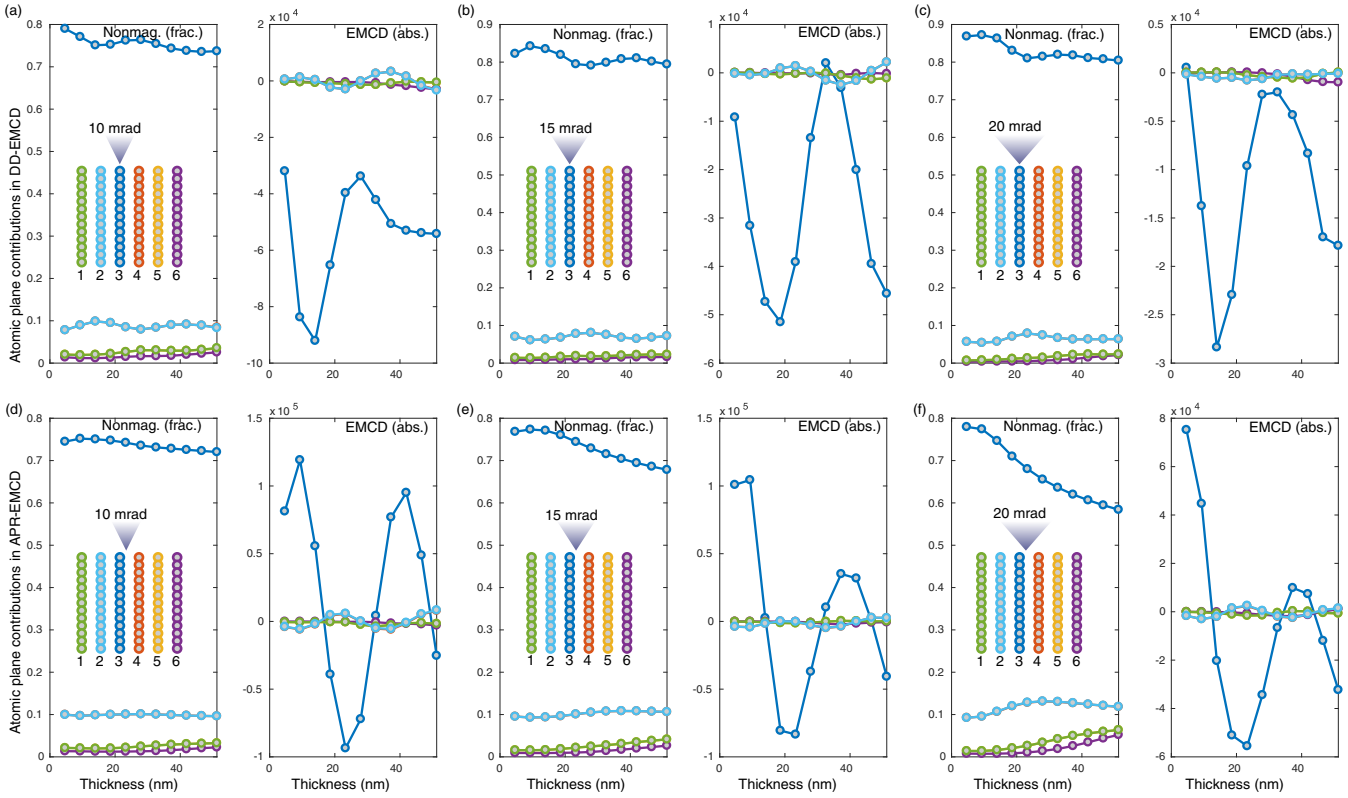

FIG. 8. Summary of the atomic plane contributions as a function of sample thickness and convergence semiangle for both DD-EMCD (upper panels) and APR-EMCD (bottom panels) geometries. The nonmagnetic signal, being always positive, is plotted as a fractional intensity, while the EMCD signal is shown in absolute numbers. Beam positions and coloring of the individual plane contributions are visualized in the insets.

originates from the other planes. As in the DD method, the contributions of the next-nearest-neighboring planes are negligible (<5%).

The profile of the EMCD signal in the APR-EMCD geometry is qualitatively different from the DD geometry. The EMCD signal is zero at the position of atomic planes and also in the middle between them. The total EMCD signal itself shows sinelike oscillations, antisymmetric with respect to atomic planes. The peak value of the EMCD is typically close to the theoretically expected $\pm\frac{d}{4}$, where d is the lattice spacing. Its slight shift is caused by different dynamical diffraction effects at different beam positions, which might locally enhance/suppress the EMCD signal as the sample thickness is increasing. However, the antisymmetry and position of nodes is fixed by symmetry constraints.

Individual lattice plane contributions also have an antisymmetric shape with respect to the center of the plane. A positive peak of a particular plane contribution reaches the negative peak of the neighboring plane, resulting in a partial cancellation of the total EMCD signal. In consequence, the peaks of the total EMCD have approximately 14% lower amplitude than the peaks of the individual lattice plane contributions. Since the magnetic signal in APR-EMCD is extracted on the sides of the atomic plane, within a specific spatial integration region—let us say $\sigma_{+\frac{d}{4}}$—there are different contributions from all atomic planes. Yet, the contributions from planes further than about 3 Å from the EMCD extraction region are all negligible (<2%). In an actual experiment, one extracts the EMCD as a difference of $\sigma_{+\frac{d}{4}}$ and $\sigma_{-\frac{d}{4}}$, and that symmetrizes the contributions of neighboring atomic planes and also reduces their relative weight; see Fig. 8 and the related discussion below.

In the case of APR-EMCD, the contrast remains well defined only for the nonmagnetic component. For a magnetic signal, it would require a different definition due to the alternating sign of EMCD as a function of beam position. For this reason, we refrain from discussing the contrast of the EMCD signal and only discuss the qualitative behavior of the contrast of the nonmagnetic signal, as summarized in Table I.

TABLE I. Contrast for nonmagnetic signals of APR-EMCD and DD-EMCD setups and magnetic signal of DD-EMCD. The contrast is computed as a difference between maximal and minimal amplitude weighted by the maximal amplitude.

t (nm)	α (mrad)	APR	DD	DD-EMCD
9.33	10	0.357	0.208	0.307
	15	0.475	0.136	0.845
	20	0.472	0.231	0.926
18.65	10	0.300	0.010	0.256
	15	0.412	0.169	0.785
	20	0.417	0.154	0.886
27.98	10	0.307	0.139	0.413
	15	0.418	0.205	0.334
	20	0.417	0.274	0.801

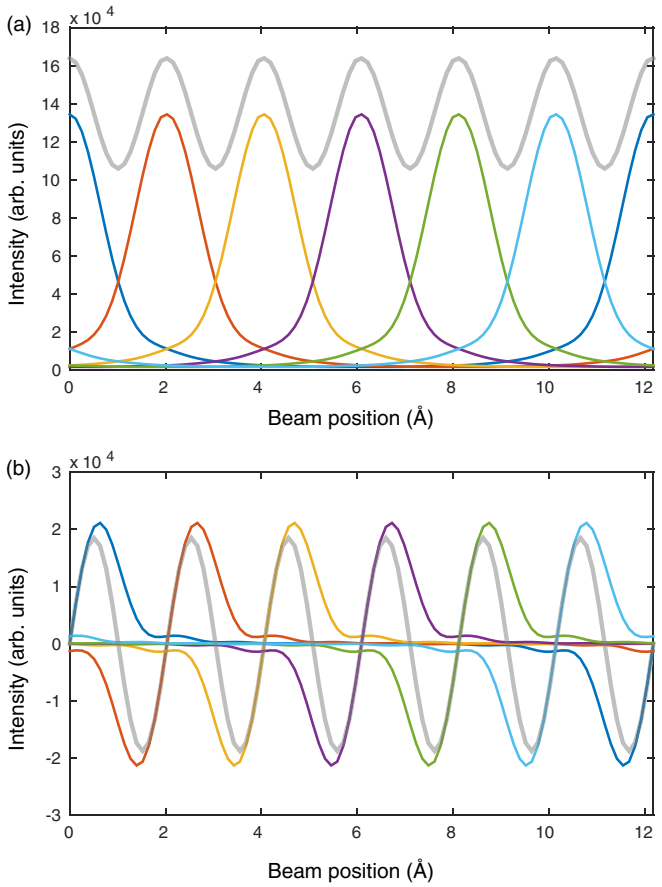

FIG. 9. Results simulated for the APR-EMCD setup. Intensity profiles of the (a) nonmagnetic and (b) magnetic component of the inelastic scattering cross section for a probe with 10 mrad convergence semiangle and sample thickness of 9.3 nm. The thick gray line marks the total profile and colored lines mark the six individual plane contributions.

The contrast generally stays between 30% and 50%. As expected, at the smallest considered convergence semiangle for 10 mrad, the contrast is lowest. It improves as we increase the convergence semiangle to $\alpha = 15$; however, no further improvement is reached for $\alpha = 20$ mrad, which might be caused by increased beam spreading during its propagation.

Delocalization of the magnetic and nonmagnetic signal in the APR-EMCD is summarized in the bottom panels of Fig. 8. The nonmagnetic signal is obtained as a sum of $\sigma_{+\frac{d}{4}}$ and $\sigma_{-\frac{d}{4}}$, while the EMCD signal is obtained as their difference. The spatial integration ranges [Fig. 1(d)] were $(\frac{25d}{8}, \frac{27d}{8})$ and $(\frac{21d}{8}, \frac{23d}{8})$ for $\sigma_{\pm\frac{d}{4}}$, respectively.

For the nonmagnetic signal component, within a range of thicknesses practical for EMCD measurements, over 70% of the intensity comes from the closest plane. The exact value slightly drops from approximately 75% at the smallest sample thickness down to 60% at the largest considered thickness. Approximately 10% comes from each of the nearest planes, numbers 2 and 4, and this value remains relatively constant throughout the range of parameters. Contributions of the plane numbers 1 and 5 are rather minor, though not negligible, especially for larger thicknesses where they reach up to 6% at the largest thickness and convergence angle. The most distant plane from the integration region, plane 6, shows between 0.8%–5% contribution to the total intensity. Summarizing, on average about 70% of intensity comes from the nearest plane and, except for the largest convergence angles and thicknesses, adding contributions of the plane numbers 2, 3, and 4 together covers above 90% of the total intensity. The rest comes from more distant planes. Compared to the DD-EMCD, the beam spreading is more pronounced here, increasingly so with larger convergence angles. That can be attributed to the fact that for APR-EMCD, the regions from which $\sigma_{\pm\frac{d}{4}}$ is extracted are displaced from atomic planes and therefore the channeling via the atomic plane is less efficient.

The delocalization of the magnetic signal is more intricate. The EMCD signal is still visibly dominated by the contribution from the closest plane number 3. However, it crosses zero several times for all considered convergence angles. Whenever this happens, the EMCD signal becomes very weak and delocalized. For this reason, in APR-EMCD experiments, it appears to be more crucial to choose an appropriate sample thickness for measurements. For our system, with systematic row index $\mathbf{G} = (110)$, this appears to be near 10 or 25 nm, respectively. In this sense, in the APR-EMCD approach, one pays for the advantages of larger detector span and single spectrum image acquisition by somewhat higher sensitivity to sample thickness and a bit reduced locality of the EMCD signal. Nevertheless, for suitable sample thicknesses, the EMCD signal remains strongly dominated by contributions from the nearest atomic plane, offering a similar degree of localization of the magnetic signal as DD-EMCD.

V. INDIVIDUAL ATOMIC CONTRIBUTIONS AND DOUBLE-CHANNELING EFFECTS

Above, we have focused on the net and plane-resolved magnetic and nonmagnetic signals. In this section, we make a more explicit use of the capability of MATS.V2 to yield the contributions of individual atoms to the net signal. By studying individual contributions, we can get a deeper insight into the role of (double) channeling and the localization of the signal. Figure 10 shows contributions of individual atoms to the net magnetic signal for APR-EMCD and DD-EMCD at five different sample thicknesses. One can clearly observe the Pendellösung oscillations and also strong double-channeling effects, particularly in the case of DD-EMCD. However, a quantitative evaluation of the graph is challenging due to the wealth of information. In order to facilitate the understanding of the z-resolved signal contributions, we reduce the parameter space by clustering the atomic contributions in bins along the z direction. A natural choice for bin size is the length of the c axis of the supercell, 2.33 nm, guaranteeing that each bin will contain the same number of atoms. In the x direction, as before, we separate the contributions of individual atomic planes.

First, we direct our attention towards the role of double channeling in both the DD-EMCD and APR-EMCD measurements. For that purpose, we computed the x,z-resolved contributions to the magnetic and nonmagnetic signal at a convergence angle of 10 mrad and the three different thicknesses. We consider the beam positioning at maximal EMCD

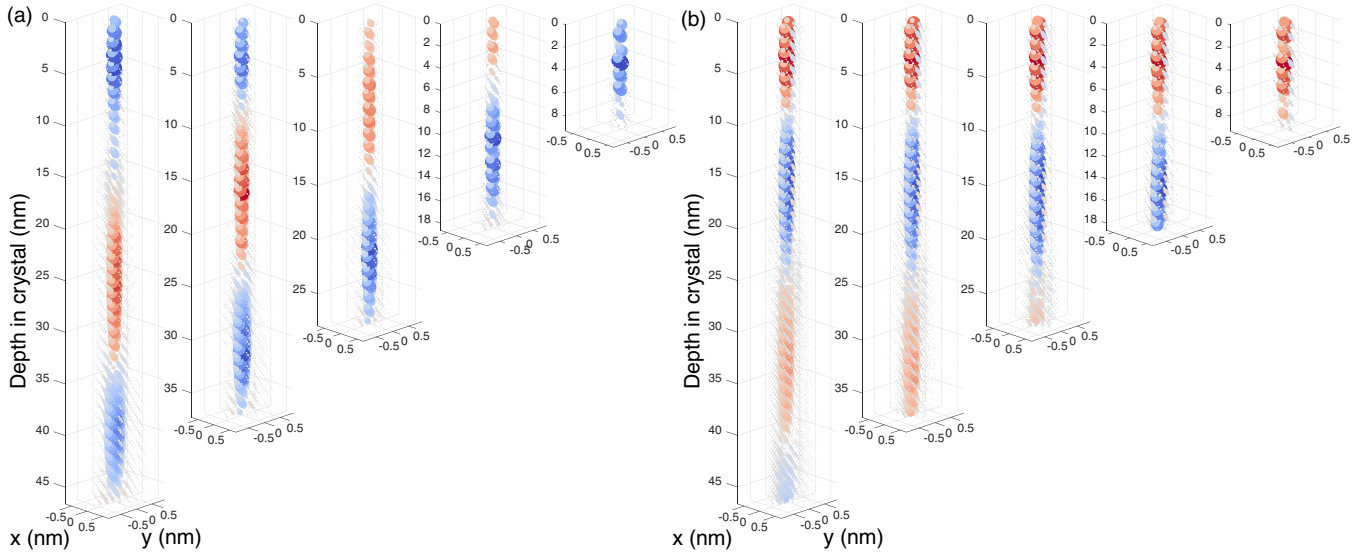

FIG. 10. Contributions of individual atoms in the supercell to the net magnetic signal at three different thicknesses for DD-EMCD (a) and APR-EMCD (b) at $\alpha = 10$ mrad. The size and color of the spheres indicates the size of the contribution; red colors indicate positive contributions, and blue colors indicate negative contributions.

strength near the third plane, i.e., $3d$ for DD-EMCD and $\frac{13}{4}d$ for APR-EMCD, respectively. For DD, the nonmagnetic signal was computed as the summed signal from all four detector positions. The resulting depth profiles of the magnetic signals are shown in Fig. 11, and the nonmagnetic signals are depicted in Fig. 12. While signals originating from individual xz bins show only minor differences between the three different thicknesses for APR-EMCD, strong differences, up to inversion of the contributions sign, are observed for the DD setting. We attribute it to the shape and range of the detection area in the diffraction plane. The DD-EMCD signal is composed of signals acquired in four different detection regions. Double channeling moves electrons in and out of the individual detection regions, as the inelastically scattered beam electrons propagate through the rest of the sample. This will have less influence on the APR-EMCD, where a large and continuous rectangular detector is used.

As expected, we observe the effect of electron channeling, when comparing the localization of the arising signals comparing on-plane and off-plane beam positions. In Fig. 13, the signals for DD and APR for beam positioning in between the atomic planes with a convergence angle of 20 mrad are displayed. As already pointed out above, the delocalization of the signal increases with larger thicknesses. When compared to Figs. 11 and 12, one observes that the proximity to the atomic planes leads to a much better localization of the signal. Where the signal originates mostly from a single atomic plane for a beam positioned on-plane, the off-plane positioning distributes major contributions to the signal over four planes for larger thicknesses.

Figure 13 also gives a different perspective to the Pendellösung oscillations for EMCD: while we observe the periodic fluctuations in the case of a more localized signal, i.e., in proximity of the atomic planes, the fluctuations are more intricate further away from the nearest lattice planes. The cancellation of contributions from the same depth with opposing signs dominates the depth distribution of the EMCD signal. In cases when the sample is not homogeneous along the x axis, these contributions may no longer cancel, leading to local changes of the observed strength of the magnetic signal. Since these effects are strongly dependent on (double) channeling, the question of how this will influence measurements

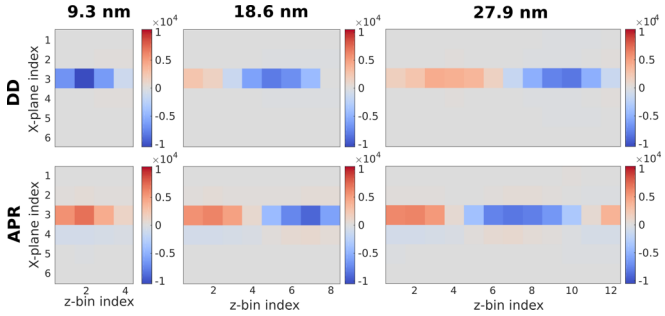

FIG. 11. x,z-resolved magnetic signal from DD (beam placed at $3d$) and APR-EMCD (beam positioning at $\frac{13}{4}d$), $\alpha = 10$ mrad.

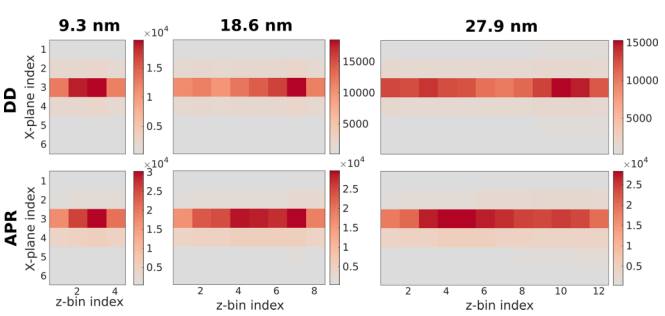

FIG. 12. x,z-resolved nonmagnetic signal from DD (beam placed at $3d$) and APR-EMCD (beam positioning at $\frac{13}{4}d$), $\alpha = 10$ mrad.

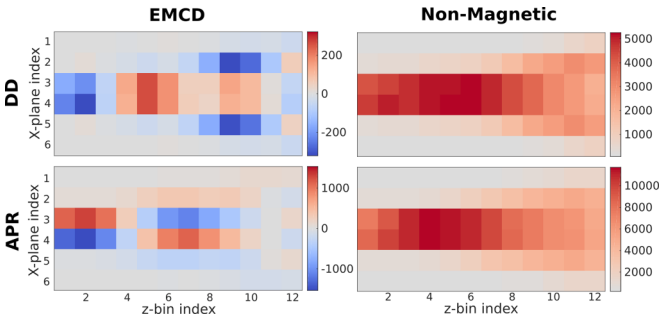

FIG. 13. Left: x,z-resolved magnetic signal for DD (top) and APR (bottom) when beam is placed at $\frac{14}{4}d$. Right: Corresponding nonmagnetic signals. Sample thickness 27.9 nm, $\alpha = 10$ mrad.

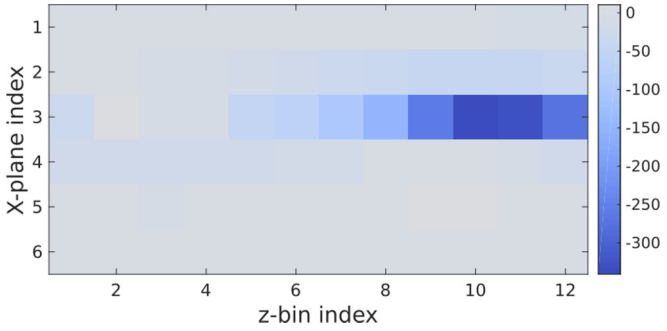

FIG. 14. x,z-resolved nonmagnetic signal for DD setup when the beam is placed at $\frac{13}{4}d$.

in the proximity of, e.g., magnetic interfaces naturally arises. This calls for an investigation of a multilayer structure model, which we leave for a separate study.

We conclude this section with a curious observation: it is possible to tune the depth from which the magnetic or nonmagnetic signal originates. In Fig. 14, we show the nonmagnetic signal obtained by applying the DD procedure to the nonmagnetic signal from the four detector positions, as in Fig. 7(c). As anticipated, the signal is weak; however, it is strongly localized at a specific depth of the sample. This suggests that by a suitably chosen range of detection angles, one might be able to isolate signals from specific depths in the crystal. As above, we leave a more general exploration of this finding for a future study.

VI. CONCLUSIONS

We have calculated the degree of localization of the magnetic (EMCD) signal in experiments with an atomic-size electron probe in three-beam orientation. The EMCD signal strength oscillates as a function of thickness and at certain nonzero thicknesses it can approach, or even cross, zero. In these situations, the magnetic signal is weak and strongly delocalized. However, when such sample thicknesses are avoided, there is a remarkably strong localization of the magnetic signal within the closest atomic plane. We have thus provided a theoretical support for the capability of the EMCD method to map the changes of magnetic properties with atomic plane spatial resolution.

Our simulations reveal strong double-channeling effects influencing the strength of the EMCD signal, particularly in the classical DD-EMCD setup. Double-channeling effects are much weaker in the APR-EMCD setup, presumably owing to a large rectangular detector used in APR-EMCD spanning a large area of the selected diffraction half plane.

Beam spreading sensitively depends on its positioning. When the beam is centered on the atomic plane, it remains rather strongly confined there, spreading only within the atomic plane. A beam centered in between planes spreads in both lateral directions and, consequently, the magnetic signal observed there is also more delocalized, with up to four atomic planes having a non-negligible contribution to the total EMCD signal. For visualization, we have used a diverging color map developed by Moreland [27].

ACKNOWLEDGMENTS

We thank the Swedish Research Council, the Göran Gustafssons Foundation, and the Center of Interdisciplinary Mathematics at Uppsala University for financial support. Calculations were done using the Swedish National Infrastructure for Computing (SNIC) on the Triolith cluster of National Supercomputer Center (NSC) at Linköping University.

[1] A. Howie, J. Microsc. Oxford **117**, 11 (1979).
[2] H. Kohl and H. Rose, Adv. Electron. Electron Opt. **65**, 173 (1985).
[3] D. A. Muller and J. Silcox, Ultramicroscopy **59**, 195 (1995).
[4] M. P. Oxley and L. J. Allen, Phys. Rev. B **57**, 3273 (1998).
[5] A. R. Lupini and S. Pennycook, Ultramicroscopy **96**, 313 (2003).
[6] P. Schattschneider, S. Rubino, C. Hébert, J. Rusz, J. Kuneš, P. Novák, E. Carlino, M. Fabrizioli, G. Panaccione, and G. Rossi, Nature (London) **441**, 486 (2006).
[7] J. C. Idrobo, J. Rusz, J. Spiegelberg, M. A. McGuire, C. T. Symons, R. Raju Vatsavai, C. Cantoni, and A. R. Lupini, Adv. Chem. Struct. Imaging **2**, 5 (2016).
[8] J. Rusz, S. Muto, J. Spiegelberg, R. Adam, K. Tatsumi, D. E. Bürgler, P. M. Oppeneer, and C. M. Schneider, Nat. Commun. **7**, 12672 (2016).
[9] T. Thersleff, J. Rusz, B. Hjörvarsson, and K. Leifer, Phys. Rev. B **94**, 134430 (2016).
[10] H. Lidbaum, J. Rusz, A. Liebig, B. Hjörvarsson, P. M. Oppeneer, E. Coronel, O. Eriksson, and K. Leifer, Phys. Rev. Lett. **102**, 037201 (2009).
[11] P. Schattschneider, M. Stöger-Pollach, S. Rubino, M. Sperl, Ch. Hurm, J. Zweck, and J. Rusz, Phys. Rev. B **78**, 104413 (2008).
[12] J. Salafranca, J. Gazquez, N. Perez, A. Labarta, S. T. Pantelides, S. J. Pennycook, X. Batlle, and M. Varela, Nano Lett. **12**, 2499 (2012).
[13] S. Schneider, D. Pohl, S. Löffler, J. Rusz, D. Kasinathan, P. Schattschneider, L. Schultz, and B. Rellinghaus, Ultramicroscopy **171**, 186 (2016).
[14] J. Rusz, Ultramicroscopy **177**, 20 (2017).

[15] J. Rusz, S. Muto, and K. Tatsumi, Ultramicroscopy **125**, 81 (2013).
[16] J. Rusz, S. Bhowmick, M. Eriksson, and N. Karlsson, Phys. Rev. B **89**, 134428 (2014).
[17] A. Weickenmeier and H. Kohl, Philos. Mag. B **60**, 467 (1989).
[18] A. Weickenmeier and H. Kohl, Acta Crystallogr. Sect. A **47**, 590 (1991).
[19] S. K. Mohanlal, J. Phys. C: Solid State Phys. **12**, L651 (1979).
[20] J. Rusz, S. Rubino, and P. Schattschneider, Phys. Rev. B **75**, 214425 (2007).
[21] B. Warot-Fonrose, F. Houdellier, M. J. Hytch, L. Calmels, V. Serin, and E. Snoeck, Ultramicroscopy **108**, 393 (2008).
[22] J. Rusz, S. Rubino, O. Eriksson, P. M. Oppeneer, and K. Leifer, Phys. Rev. B **84**, 064444 (2011).
[23] O. Krivanek, N. Dellby, M. F. Murfitt, M. F. Chisholm, T. J. Pennycook, K. Suenaga, and V. Nicolosi, Ultramicroscopy **110**, 935 (2010).
[24] R. F. Egerton, Ultramicroscopy **107**, 575 (2007).
[25] J. Rusz, O. Eriksson, P. Novák, and P. M. Oppeneer, Phys. Rev. B **76**, 060408(R) (2007).
[26] L. Calmels, F. Houdellier, B. Warot-Fonrose, C. Gatel, M. J. Hÿtch, V. Serin, E. Snoeck, and P. Schattschneider, Phys. Rev. B **76**, 060409(R) (2007).
[27] K. Moreland, in *Advances in Visual Computing. ISVC 2009. Lecture Notes in Computer Science*, edited by G. Bebis *et al.* (Springer, Berlin, 2009), Vol. 5876, p. 92.